Tribol Lett (2015) 57:23
DOI 10.1007/s11249-014-0451-8

ORIGINAL PAPER

Linear Elastic Fracture Mechanics Predicts the Propagation Distance of Frictional Slip

David S. Kammer · Mathilde Radiguet · Jean-Paul Ampuero · Jean-François Molinari

Received: 15 August 2014 / Accepted: 6 December 2014 / Published online: 23 January 2015

Abstract When a frictional interface is subject to a localized shear load, it is often (experimentally) observed that local slip events propagate until they arrest naturally before reaching the edge of the interface. We develop a theoretical model based on linear elastic fracture mechanics to describe the propagation of such precursory slip. The model's prediction of precursor lengths as a function of external load is in good quantitative agreement with laboratory experiments as well as with dynamic simulations, and provides thereby evidence to recognize frictional slip as a fracture phenomenon. We show that predicted precursor lengths depend, within given uncertainty ranges, mainly on the kinetic friction coefficient, and only weakly on other interface and material parameters. By simplifying the fracture mechanics model, we also reveal sources for the observed nonlinearity in the growth of precursor lengths as a function of the applied force. The discrete nature of precursors as well as the shear tractions caused by frustrated Poisson's expansion is found to be the dominant factors. Finally, we apply our model to a different, symmetric setup and provide a prediction of the propagation distance of frictional slip for future experiments.

Keywords Stick-slip · Friction mechanisms · Unlubricated friction · Linear elastic fracture mechanics

D. S. Kammer · M. Radiguet · J.-F. Molinari (✉)
Computational Solid Mechanics Laboratory, IIC-ENAC, IMX-STI, Ecole Polytechnique Fédérale de Lausanne, EPFL, 1015 Lausanne, Switzerland
e-mail: jean-francois.molinari@epfl.ch

J.-P. Ampuero
Seismological Laboratory, California Institute of Technology, Pasadena, CA, USA

1 Introduction

Recent laboratory experiments have shown that nominally flat interfaces between solids under a localized quasi-static shear load may present local slip precursors well before global sliding [1, 2]. These findings on the transition from sticking to sliding have attracted wide attention [3–8]. They have important implications in engineering as well as earthquake science, where spatially concentrated loads appear at the base of the seismogenic zone of most faults, and ruptures propagate over parts of the interfaces [9, 10]. In the experiments, two PMMA (acrylic glass) blocks are brought into contact under a constant normal load F_N. A shear load F_S is applied to the top block (slider) via a pusher located close to the interface (Fig. 1a). In this side-driven setup, local slip fronts nucleate episodically at the trailing edge and propagate over parts of the interface. The precursor length is proportional to the applied load until approximately the middle of the interface. From this point on, the propagation distance increases as a function of the applied load considerably faster (*e.g.*, see experimental data from [1] shown in Fig. 4a). Once a slip event propagates over the entire interface, global sliding occurs.

The remarkable increase of precursor lengths and its nonlinear relation to the applied shear force F_S were shown to be highly reproducible and, if normalized by sample length and normal force, unique and independent of the slider geometry (length or height), of the normal load, and of the pusher position [1, 4]. In essence, episodic nucleation and subsequent spontaneous arrest of precursor fronts arise from the spatial concentration of interface stresses induced by the applied load [11]. Several numerical models, one-dimensional spring-mass chains with arbitrary normal loads [2, 6] as well as two-dimensional spring-mass models [4], were proposed to simulate the mechanics of

precursors and to analyze the relation between the normalized precursor length and the measured macroscopic force ratio F_S/F_N. They confirmed experimental observations showing the absence of influence of the slider geometry and produced nonlinear evolution of the precursor length. However, none of these numerical simulations provided quantitative comparison to experimental data. The main reasons being inconsistent interface stresses due to the discrete nature [2, 4, 6] or the one-dimensional geometry [2, 6] of these models.

In addition to numerical models, only few theoretical approaches have been proposed so far. A quasi-static one-dimensional model [3] applied a simplified stress criterion, inspired by Griffith's energetic criterion, to study the kinematics of the transition from static to stick-slip friction and showed that it is dominated by the system instead of the small-scale parameters. Another analytical model [6] applied a reverse approach. Given a precursor length, they describe the interface stresses after precursor arrest and compute the associated macroscopic shear force by integration of the interface shear tractions. Even though these theoretical models offer interesting intuition about the propagation length of precursors, they do not give new insights about the mechanics of friction nor do they provide quantitative comparison with experiments. There are several causes to this discrepancy. As for the numerical simulations, the one-dimensional geometry and the arbitrary initial stress states can result in inconsistent predictions. Moreover, the simplistic propagation criteria and the use of post-precursor instead of pre-precursor stress states are additional limitations of existing models.

In this study, we present a theoretical model based on linear elastic fracture mechanics (LEFM) that predicts the kinematics of slip precursors at frictional interfaces. Such LEFM approaches have long been used in earthquake modeling [12–14], and recently, experimental evidence was provided by measurements of LEFM strain fields around Sub-Rayleigh slip fronts [15]. We here develop this concept into a quantitative model that incorporates the continuum nature of fracture mechanics theory as well as interface stress states resulting from the exact system geometry. The aim of this model is to be as simple as possible while comprising the essential features of fracture mechanics theory (more precisely LEFM) and addressing the shortcomings of previous theoretical models. With this approach, we study the link between meso-scale properties and the macro-scale response of a solid-body system containing a frictional interface. Friction mechanisms acting at even smaller scales (i.e., atomic scale) are incorporated in a local (meso-scale) friction law.

Specifically, we use real interfacial stress states from a two-dimensional geometry to provide a prediction of the precursor length based on the shear load measured before the slip event and compare our results quantitatively with experimental data. In addition, we analyze the influence of several material and interface parameters, which has not been done before, and point out various sources of the precursor length nonlinearity. This analysis is further extended by considering simplifications of our model, which provide a fundamental understanding of the origin of the nonlinearity of the precursor length evolution.

2 Model

As in [1], the studied system is modeled by a rectangular thin plate of length $L = 200$ mm, height $H = 75$ mm and thickness $b = 6$ mm, in contact with a much thicker deformable base block of dimensions $300 \times 30 \times 27$ mm. A pusher of width $w_p = 5$ mm is applied at height $h_p = 6$ mm from the interface. The material properties are assumed to be viscoelastic, with Poisson's ratio ν, viscous E_v and static E_∞ Young's moduli. The resulting instantaneous Young's modulus is given by $E_0 = E_v + E_\infty$. The long-term behavior of the modeled system, for instance the stress state of the interface due to the external loading, is computed using the static Young's modulus E_∞. The dynamic mechanisms, as for example the stress drop, are, however, affected by the instantaneous Young's modulus. The viscous time scale, as it is usually given by the viscosity parameter η, is not explicitly incorporated into this model due to the clear time-scale separation of the studied problem. In fact, the propagation duration of a typical slip front is considerably shorter than the viscous time scale, and the time between two precursors is considerably longer. A linear slip-weakening friction law [16, 17] is applied at the interface, describing the frictional strength as

$$\tau^s(\delta, x) = \max(\mu_k, \mu_s + \delta/d_c(\mu_k - \mu_s))\sigma(x)\,, \qquad (1)$$

where μ_s and μ_k are the static and kinetic friction coefficients, d_c is the characteristic weakening length, δ is the local interface slip, $\sigma(x)$ is the contact pressure and x is the coordinate along the interface. More advanced friction laws, such as velocity-weakening and velocity-strengthening friction, have been used in the past to model precursor mechanics at PMMA interfaces [5, 18–21]. Even though these models describe well the propagation of frictional slow fronts, they are not indispensable to model the propagation distance of precursors, as shown with dynamic finite-element simulations using slip-weakening friction [22]. Here, the emphasis is on simplicity and the slip-weakening friction law enables simple determination of the interface's fracture toughness, which is essential to LEFM theory.

The unruptured tractions at the interface are computed by static finite-element simulations. An applied normal displacement resulting in a unit normal force on the top boundary leads to a normal traction $\sigma_N(x)$ satisfying the following condition $b\int_0^L \sigma_N(x)\mathrm{d}x = 1\,\mathrm{N}$. The resulting contact pressure (Fig. 1b) is approximately uniform in the central 80 % of the interface and presents singularities at the edges due to the perfect rectangular shape of the specimen. Poisson's lateral expansion is frustrated at the interface by the frictional strength leading to a shear traction $\tau_N(x)$, which is approximately linear and symmetric with respect to the center point of the interface. Similarly,

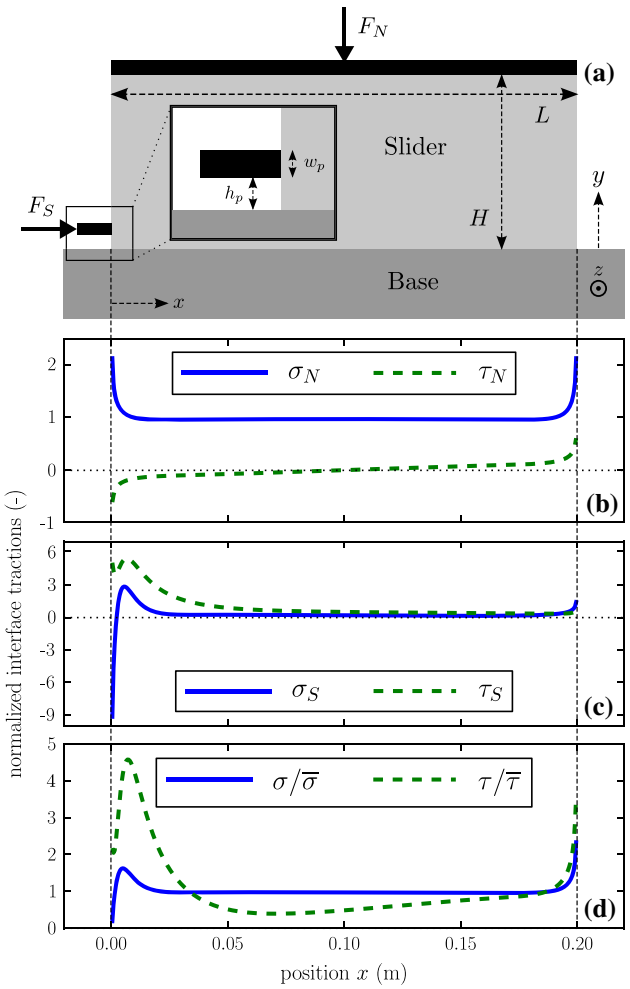

Fig. 1 **a** Setup of the side-driven system. A thin slider is pressed by a constant normal load F_N onto a thicker base block. The rigid block (shown in *black*) used to apply the normal load is frictionless and does not allow for rotation. A pusher applies a slowly increasing shear load F_S to the slider. (*inset*) Zoom on the pusher. **b** Static stress state at the interface for an applied normal load. Note the convention of positive σ for compression. **c** Static stress state at the interface for an applied unit shear load. **d** Interface stresses for an unruptured linear combination of both loadings with $F_N = 5F_S$ and normalized by the average interface stress

$\sigma_S(x)$ and $\tau_S(x)$ result from an applied pusher displacement leading to a unit horizontal force and satisfy therefore $b\int_0^L \tau_S(x)\mathrm{d}x = 1\,\mathrm{N}$. As shown in Fig. 1c, $\tau_S(x)$ presents a maximum close to the trailing edge, which will eventually lead to the initiation of precursors. Due to the fixed top boundary and the Poisson's effect, the contact pressure induced by the shear load contributes to the normal force, *i.e.*, $b\int_0^L \sigma_S(x)\mathrm{d}x \neq 0\,\mathrm{N}$.

It is important to note that although the unruptured interface tractions are computed by static finite-element simulations, the following model is theoretical and independent of numerical simulations. Any interface stress state, also experimental data, could be used as starting point for our model.

Once the unruptured interface tractions, caused by external loadings, are known, the effective interface tractions are then modeled by linear superposition of these tractions and the stress drops due to previous interface ruptures. The normal $\sigma_r(x,t)$ and shear $\tau_r(x,t)$ tractions after $r-1$ precursors, for any $F_N(t)$ and $F_S(t)$, and after viscous relaxation are given by

$$\sigma_r(x,t) = \tilde{F}_N(t)\,\sigma_N(x) + \tilde{F}_S(t)\,\sigma_S(x) \tag{2}$$

$$\tau_r(x,t) = \tilde{F}_N(t)\,\tau_N(x) + \tilde{F}_S(t)\,\tau_S(x) + \frac{E_\infty}{E_0}\sum_{i=1}^{r-1} \Delta\tau_i(x)\,, \tag{3}$$

with $\tilde{F}_N(t)$ and $\tilde{F}_S(t)$ ensuring that the macroscopic normal and shear loads are always equal to $F_N(t)$ and $F_S(t)$, *e.g.*, $b\int_0^L \sigma_r(x,t)\mathrm{d}x = F_N(t)$ and $b\int_0^L \tau_r(x,t)\mathrm{d}x = F_S(t)$. Note that $\tilde{F}_N(t) \neq F_N(t)$ because $b\int_0^L \sigma_S(x,t)\mathrm{d}x \neq 0\,\mathrm{N}$ as mentioned above. The change in the shear tractions caused by interface rupture i is introduced as $\Delta\tau_i(x)$, while contact pressure changes are neglected. As shown by [22, 23], the bulk material's viscoelasticity results in a partial restitution of pre-rupture shear tractions. Given that the viscous time scale is faster than the duration between two precursors, full viscoelastic restitution is assumed and the stress drops can therefore be multiplied by E_∞/E_0. Furthermore, a non-adhesion condition defines that where $\sigma_r(x) \leq 0$ we impose: $\sigma_r(x) = 0$ and $\tau_r(x) = 0$. An example of an effective stress state without a stress drop is shown in Fig. 1d. The contact pressure is rather uniform, while the shear traction presents an important peak close to the trailing edge, which is at the origin of slip nucleations.

Considering local slip events as interface ruptures, we model their propagation using LEFM [24], which implies that every rupture modifies the stress state of the interface behind as well as ahead of its tip. An example of how shear tractions change during a slip event is shown in Fig. 2a for a rupture with arrest position $x/L = 0.55$. The shear

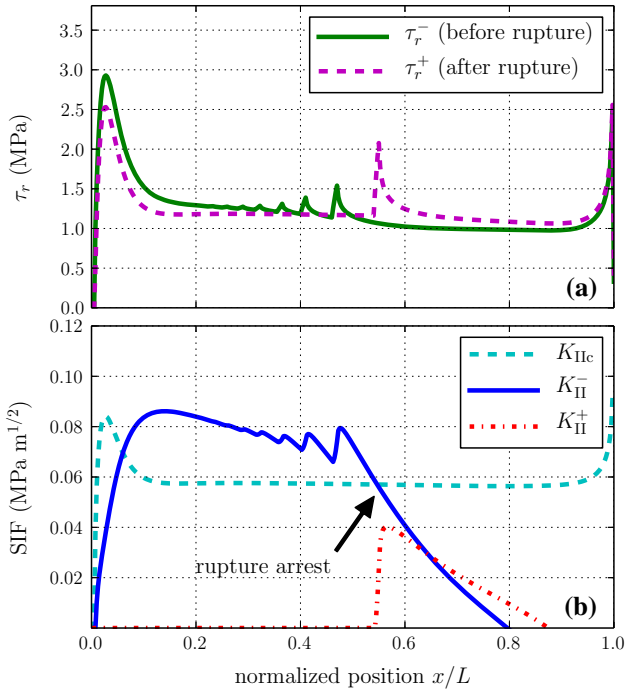

Fig. 2 **a** Interfacial shear tractions before and after an interface rupture. These tractions are obtained by 13 iterations of Eqs. 3 and 4 and based on unruptured interface tractions τ_N and τ_S originally computed by static finite-element simulations. **b** Fracture toughness K_{IIc} and stress intensity factor K_{II}^- (*before*) and K_{II}^+ (*after*) the rupture shown in **a**

tractions before and after an interface rupture (in time) are denoted with a superscript $-$ and $+$, respectively. The arrest of the precursor creates a peak at $x/L = 0.55$ and a square root decrease in shear tractions for $x/L > 0.55$ (see τ_r^+). The peaks in τ_r^- at $x/L = 0.3 - 0.5$ are the remains of stress concentrations of previous precursors. After the current rupture, they are erased due to the linear slip-weakening friction law (see τ_r^+) and will partially reappear over time. This effect was shown to be the result of the bulk's visco-elasticity [22, 23].

The tractions before and after the rupture r are linked by the stress change $\Delta\tau_r(x)$ through $\tau_r^+(x) = \tau_r^-(x) + \Delta\tau_r(x)$. The stress τ_r^- is equal to $\tau_r(x)$ (Eq. 3) for F_N and F_S at the time of the rupture. The stress $\tau_r^+(x)$ is the result of the rupture and can be separated into three different areas as described below.

At the rupture tip, there is a process (weakening) zone, where $\delta < d_c$ and in which the shear traction drops from the static frictional strength $\tau^s(0,x)$ to the kinetic strength $\tau^s(d_c,x)$. A linear slip-weakening friction law results within the process zone in a nonlinear shear traction distribution, which, for reasons of simplicity, is here approximated by a linear function. The size of a static linear process zone is given by $w = 9\pi K_{\mathrm{II}}^2(l)/[32\,\sigma_r^2(l)\,(\mu_s - \mu_k)^2]$ [16], where l is the arrest position of the precursor and K_{II} the mode II stress intensity factor. The leading end of the process zone is at $x = l_a$ and the trailing end at $x = l_a - w = l_b$. The position l_a of the leading end is determined by the stress concentration as defined below, which always results in a process zone that satisfies $l_b < l < l_a$.

Behind the process zone, the stress state is imposed by the friction law (Eq. 1). Because $\delta > d_c$ everywhere, we can write $\tau_r^+(x) = \tau^s(d_c,x) = \mu_k\sigma_r(x)$ for $x < l_b$.

Ahead of the slip event appears a stress concentration caused by the stress drop occurring behind the rupture tip. The stress change ahead is given in first-order approximation as $\Delta\tau_r(x) \approx K_{\mathrm{II}}(l)/\sqrt{2\pi(x-l)}$. Because frictional rupture does not allow for stress singularities, the frictional strength limits the maximal shear traction, similar to the assumption of a small plastic zone size in fracture mechanics. Therefore the position of the leading end of the process zone is determined such that $\mu_s\sigma_r(l_a) = \tau_r^-(l_a) + K_{\mathrm{II}}(l)/\sqrt{2\pi(l_a - l)}$.

This is only a simplified approximation to the correct description of the stress state around a cohesive crack. In fact, the details have no significant effect on the precursor load–length relation studied here, and even neglecting entirely the process zone results in virtually the same observations with isolated shorter slip events that do not affect the load–length relation of the expanding precursors.

The stress change caused by an interface rupture can therefore be summarized as

$$\Delta\tau_r(x) = \begin{cases} \dfrac{K_{\mathrm{II}}(l)}{\sqrt{2\pi(x-l)}} & \text{for } x > l_a \quad (4a) \\ \Delta\tau_r(l_b) + \dfrac{x - l_b}{w}\,\Delta\tau_{pz} & \text{for } l_b < x < l_a \quad (4b) \\ \mu_k\sigma_r(x) - \tau_r^-(x) & \text{for } x \le l_b\,, \quad (4c) \end{cases}$$

with $\Delta\tau_{pz} = \Delta\tau_r(l_a) - \Delta\tau_r(l_b)$. The process zone is characterized by l the arrest position of the rupture, l_a and l_b the leading and trailing end, respectively, and $w = l_a - l_b$ the process zone size. Note that $\Delta\tau_r(l_a)$ and $\Delta\tau_r(l_b)$, which are needed in Eq. (4b), are given by Eq. (4a) and Eq. (4c), respectively.

The mode II stress intensity factor for a non-uniform shear stress drop $\Delta\tau_r$ along an edge crack of length a in a semi-infinite solid can be deduced from Equation 8.3 in [25] by integration:

$$K_{\mathrm{II}}(a) = \frac{2}{\sqrt{\pi a}}\int_0^a \frac{\Delta\tau_r(s)F(s/a)}{\sqrt{1-(s/a)^2}}\mathrm{d}s \qquad (5)$$

with $F(s/a) = 1 + 0.3(1-(s/a)^{5/4})$ and $\Delta\tau_r(s) = \mu_k\sigma_r(s) - \tau_r^-(s)$ because the integration is along the crack interface and the process zone is neglected. A different

possible choice of stress intensity factor is a semi-infinite crack approaching the edge of a semi-infinite solid (Equation 9.5 in [25]). On the studied system, this stress intensity factor leads to an almost identical precursor load–length relation as in the model with Eq. 5. Only a slightly steeper curve at $l/L > 0.5$ is observed (not shown here). As $\Delta\tau_r$ is multiplied by the nonlinear factor $F(s/a)/\sqrt{1-(s/a)^2}$ over the crack face, the stress intensity factor is one possible source of nonlinearity in precursor mechanics.

Given that the slider is a thin plate, the fracture toughness is computed in the plane-stress approximation with the frictional fracture energy G by:

$$K_{\mathrm{IIc}}(x) = \sqrt{E_0\, G(x)} = \sqrt{E_0 \frac{(\mu_\mathrm{s}-\mu_\mathrm{k})d_\mathrm{c}}{2}\sigma_r(x)}\,. \tag{6}$$

The fracture toughness is computed using E_0 because the characteristic frictional weakening time is significantly smaller than the relaxation time of the viscoelastic material [26].

Neglecting any dynamic effect, the precursor length l for a given stress state of the interface is determined by the position at which the stress intensity factor becomes smaller than the fracture toughness:

$$K_\mathrm{II}^-(l) = K_{\mathrm{IIc}}(l) \quad \text{and} \quad \frac{\mathrm{d}K_\mathrm{II}^-(l)}{\mathrm{d}x} < \frac{\mathrm{d}K_{\mathrm{IIc}}(l)}{\mathrm{d}x}. \tag{7}$$

An example is shown in Fig. 2b. The stress intensity factor right after an event K_II^+ is significantly lower than K_{IIc}; hence, a finite load increment is required to nucleate the next precursor event.

Up to this point, we presented how the precursor length can be predicted for any given interface stress state. In order to complete the proposed model, we need to determine the shear force at which a slip event is expected. As the initiation of the rupture occurs at the trailing edge of the system and a rupture only propagates where the stress intensity factor is larger than the fracture toughness, we introduce a length scale l_n that represents the size of the nucleation zone, and define that the next precursor occurs when the following condition is satisfied:

$$K_\mathrm{II}^-(l_\mathrm{n}) = K_{\mathrm{IIc}}(l_\mathrm{n}) \quad \text{and} \quad \frac{\mathrm{d}K_\mathrm{II}^-(l_\mathrm{n})}{\mathrm{d}x} > \frac{\mathrm{d}K_{\mathrm{IIc}}(l_\mathrm{n})}{\mathrm{d}x}. \tag{8}$$

The slip nucleation zone size l_n acts like a seed crack to the propagation of an interface rupture and can be thought of as the stable slip zone that occurs before dynamic ruptures [27, 28]. Its size may vary from one to another slip event, but is chosen to be constant in our model. However, testing different values for l_n has shown that below a critical length, it has only a negligible influence on the precursor load–length relation. Decreasing l_n only leads to slightly less precursors. The result is only weakly sensitive to l_n because of the high gradient in K_II^- to the left of its peak point (see blue curve in Figs. 2b and 3 for $x/L<0.12$), which results from the shear stress concentration (see τ_r^- in Fig. 2a and Eq. 5). As a consequence, the critical length above which l_n affects the load–length prediction corresponds here approximately to the position of the maximum of K_II^-. In this work, we chose $l_\mathrm{n}/L = 0.06$, which is below the critical length and results in approximately the same precursor occurrence frequency as in the experiment of [1].

Before comparing our model with experimental data and studying the influence of various parameters, we here summarize the events occurring during a cycle of an interface rupture in order to provide the reader with a basic intuition of the observed phenomenon. Considering an interface stress state at which a slip event occurs (*e.g.,* Fig. 2a), a rupture propagates from the trailing (left) edge until a point where the stress intensity factor becomes smaller than the fracture toughness (Eq. 7 and Fig. 2b). Behind the rupture occurs a stress drop and ahead of the tip a stress concentration as described by Eq. 4. The stress concentrations of previous ruptures are erased because behind the process zone the friction law imposes shear tractions that depend only on the kinetic friction coefficient and the contact pressure. The viscous memory effect of the bulk material restores these

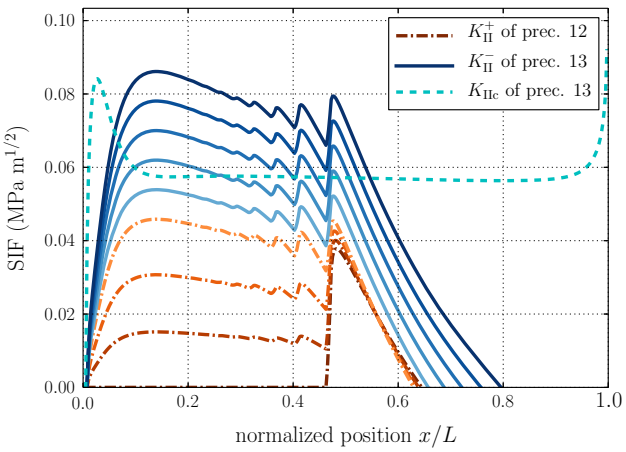

Fig. 3 The evolution of the stress intensity factor is shown during the period between two precursors. Directly after precursor 12, the stress intensity factor K_II^+ is zero along the interface and nonzero ahead of the arrest position, as shown by the *dash-dotted dark orange curve*. Viscous relaxation of the bulk material, illustrated by the *dash-dotted orange curves* going from dark to bright, leads to a partial recovery of the pre-rupture stress intensity factor. Further, the increasing external shear load lifts continuously the stress intensity factor, as shown by the *solid blue curves* going from bright to dark. When the area of $K_\mathrm{II}^- > K_{\mathrm{IIc}}$ reaches the slip nucleation zone characterized by $x \le l_\mathrm{n} = 0.06L$, the next precursor propagates. For simplicity, the effects of the viscous relaxation and the external loading are here illustrated sequentially. In reality, they occur simultaneously. However, if complete relaxation occurs between two precursors, the sequential and simultaneous approaches are equivalent (Color figure online)

concentrations partially over time [22]. Directly after the rupture and before viscous relaxation, the stress intensity factor is zero along the interface up to the arrest position (see K_{II}^{+} in Figs. 2b and 3). Thus, additional external shear loading is needed to reach a new interface stress state that allows for the propagation of a slip event. While the external loading increases, the stress intensity factor exceeds the fracture toughness first, for this particular setup, at approximately $x/L = 0.15$ and shortly after at a position close to the last arrest position (see Fig. 3). Nevertheless, no rupture initiates because the shear traction is still below the static strength, $\tau_r(x) < \tau^{\mathrm{s}}(0,x)$ (at the last arrest position due to viscous relaxation), and the stress intensity factor should be higher than the fracture toughness starting from the edge (and not solely in the middle of interface). For even higher external shear loads, the area with $K_{\mathrm{II}}^{-} > K_{\mathrm{IIc}}$ expands and once it reaches the seed crack at the edge, and satisfies Eq. 8, a new slip event occurs and the cycle starts over again.

3 Results and Discussion

3.1 Comparison to Experimental Data

In Fig. 4a, we compare the LEFM prediction (blue dots) with experimental data from [1] (gray triangles). Material parameters correspond to PMMA [29] and interface parameters are deduced from experimental measurements [1, 15, 30]: $E_\infty = 2.6$ GPa, $E_{\mathrm{v}} = 3.0$ GPa, $\nu = 0.37, \mu_{\mathrm{s}} = 0.9, \mu_{\mathrm{k}} = 0.45, d_{\mathrm{c}} = 1$ µm, and $F_{\mathrm{N}} = 3300$ N. The LEFM prediction is in good quantitative agreement with experimental data and retrieves well the nonlinearity of the length vs. load curve. It is also in good quantitative agreement with results from dynamic finite-element simulations presented in [23] (Fig. 4a, red squares). These simulations are in plane-stress (slider) and plane-strain (base) approximation with the same geometry, material and interface parameters as for the LEFM model (for more details see [23]). Further, we also confirm the observation of [4] that the slider geometry does not influence the normalized precursor length behavior by changing the slider length to $L = 0.14$ m (see cyan triangles in Fig. 4a).

The force increment between each precursor event is nearly constant in both the experimental data [1] and the prediction from the LEFM model. In the experiments, this is likely to be caused by the stress state of the interface close to the trailing edge being almost identical after each slip event. As a consequence, the slowly expanding quasi-static slip zone, which governs nucleation, reaches each time its critical length for the same force increment. In the LEFM model, this mechanism is well captured by the constant nucleation length l_n. However, the applied nucleation condition in our LEFM model is only a simplification of a considerably more complex phenomenon, which is still not well understood. For some problems, the critical nucleation length has been determined by proving the absence of a quasi-static solution for longer cracks [27, 28].

We present in Fig. 4b the influence of various material and interface properties with variations of the order of their uncertainties. The value of μ_{k} is estimated by the macroscopic force ratio $F_{\mathrm{S}}/F_{\mathrm{N}}$ measured directly after a slip event, which is often $\mu_{\mathrm{k}} \approx 0.4 - 0.45$ [1]. Introducing an

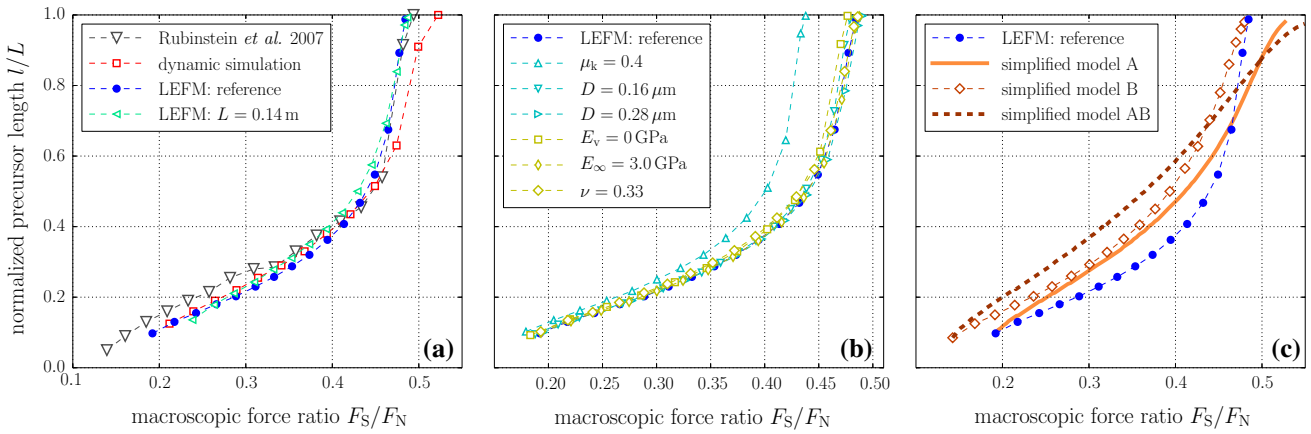

Fig. 4 Evolution of normalized precursor length with increasing macroscopic force ratio $F_{\mathrm{S}}/F_{\mathrm{N}}$. **a** Comparison of LEFM theory with experimental data from [1], and dynamic finite-element simulations from [23]. **b** Influence of different interface and material parameters. Parameters that are changed with respect to the reference case are given in the legend. The variation of the equivalent slip distance D for $\mu_{\mathrm{k}} = 0.45$ corresponds to the uncertainty range of the frictional fracture energy deduced from experiments [15]. **c** Comparison of full LEFM theory with simplified models. Model A: Traction changes due to interface ruptures are neglected (Eq. 3 is replaced by Eq. 9). Model B: Interface shear tractions due to frustrated Poisson's expansion are neglected ($\tau_{\mathrm{N}}(x) = 0$). Model AB: combination of model A and model B (Eq. 3 is replaced by Eq. 9 and $\tau_{\mathrm{N}}(x) = 0$) (Color figure online)

equivalent slip distance $D = (\mu_s - \mu_k)d_c/2$ enables us to write Eq. 6 as $K_{IIc}(x) = \sqrt{E_0 D \sigma(x)}$. According to the experiment-based estimation of the frictional fracture energy of PMMA interfaces reported in [15], the uncertainty of the equivalent slip distance can be determined to be within the range of $D = 0.22 \pm 0.06$ μm for $\mu_k = 0.45$.

With the exception of μ_k, the variations of all material and interface parameters within their uncertainties have negligible effects on the $l/L - F_S/F_N$ relation (Fig. 4b). Even neglecting entirely the viscoelasticity of the bulk material ($E_0 = E_\infty$, which leads to $E_v = 0$ GPa) does not affect the precursor behavior. This weak influence originates from the square root contribution of E_0 and D to K_{IIc}. Only a change of μ_k within its uncertainty range results in an important shift of the $l/L - F_S/F_N$ curve due to its additional contribution to K_{II} (Eqs. 4 and 5).

3.2 Test of Model Assumptions

We have shown that the LEFM model is able to produce an accurate prediction of the precursor load–length curve and reproduce the transition from the initial linear length increase to faster increase at a finite value of load. In the following, we aim at giving a more fundamental understanding of the origin of the load–length curve, by identifying several sources of the nonlinearity in this scaling. This is done by removing different components from the LEFM model.

We present in Fig. 4c a simplification of the theoretical model (denoted model A), which is based on the same LEFM approach, but where any change in the interface tractions due to slip is neglected. Equation 3 is therefore replaced by

$$\tau_r(x,t) = \tilde{F}_N(t)\,\tau_N(x) + \tilde{F}_S(t)\,\tau_S(x)\,, \qquad (9)$$

but the stress intensity factor is still computed with Eqs. 5 and (4c). Under these conditions, the discrete nature of precursors is lost. The length associated with a given macroscopic force ratio is independent of the slip history of the interface and corresponds to the length that the first precursor would reach if it is initiated at that specific loading. The loss in discreteness results in a more (but still not) linear $l/L - F_S/F_N$ relation. In this simplified model, for a given F_S, the stress drop close to the trailing edge is larger than in the reference case, resulting in a higher value of K_{II} and in longer precursors. But for $l/L > 0.7$, this effect is compensated in the full theory by the stress redistribution close to the arrest position of the previous precursor.

As noted before, the shear tractions at the interface result not only from the macroscopic shear load but also, due to frustrated Poisson's expansion, from the normal load. The influence of the latter is analyzed in model B. The shear contribution of the macroscopic normal load is removed by setting artificially $\tau_N(x) = 0 \quad \forall x$. All remaining interface tractions are kept the same as for the reference case. The resulting propagation distances reported with respect to the macroscopic force ratio are shown in Fig. 4c. For any given shear force F_S, the precursor length is longer for the simplified model B than for the reference model. For $l/L < 0.5$, this is the logic consequence of neglecting $\tau_N(x)$ which acts against the driving traction $\tau_S(x)$. Beyond the central point of the interface, the precursor lengths increase faster but still less than in the reference system, where $\tau_N(x)$ contributes to the propagation of precursors. From a global perspective, the precursor load–length curve is still nonlinear (but less than the reference model). This indicates that the interfacial shear traction resulting from frustrated Poisson's expansion is one but not the only source of nonlinearity in the system.

We also present the results of the simplified model AB, which is the combination of model A and B, where stress drops due to interface ruptures as well as shear traction caused by frustrated Poisson's expansion are neglected. As for model A, the discrete nature of precursors is lost in model AB. The precursor load–length relation, which is shown in Fig. 4c, is almost perfectly linear indicating that most sources of nonlinearity (at least for the studied system and parameter range) are eliminated from this simplified model. The nonlinear form of the stress intensity factor, which is still part of model AB, does not seem to affect the precursor propagation distance much within the length of the interface.

3.3 Insights from a Minimalistic Model

In the previous section, we simplified the LEFM model by removing different components in order to analyze their contributions to the nonlinearity of the precursor load–length relation. In this section, we apply fracture mechanics in an even simpler model.

Let us assume, in order to simplify the computation of the stress intensity factor, that the edge crack considered so far is half of a central shear crack at a weak interface of length $2L$. The interface is subjected to a linear shear load and to a point shear load at the center of the crack (see *inset* in Fig. 5). The linear shear load corresponds in the full model to the effect of the frustrated Poisson's expansion. The point load represents the localized shear load caused by the pusher. The stress drop along this interface is therefore given by

$$\Delta\tau(x) = \frac{2\tau_N^{max}}{L}\left(|x| - \frac{L}{2}\right) + F_S\,\delta(x) - \tau_d\,, \qquad (10)$$

where τ_N^{max} is the maximal shear traction (at $x = L$) due to frustrated Poisson's expansion, F_S is the amplitude of the

point load, $\delta(x)$ is the Dirac delta function and τ_d is the dynamic shear stress left behind the crack.

The stress intensity factor of a central crack of length $2a$ is found by integration of equation 5.11 of [25]:

$$K_{II}(a) = 2\sqrt{\frac{a}{\pi}}\int_0^a \frac{\Delta\tau(s)}{\sqrt{a^2-s^2}}\mathrm{d}s \tag{11}$$

$$= \sqrt{\pi a}\left[\tau_N^{\max}\left(\frac{4}{\pi}\frac{a}{L}-1\right)+\frac{2}{\pi}\frac{F_S}{a}-\tau_d\right]. \tag{12}$$

Using the same propagation criterion to predict precursor length l as for the full theory, we can write $K_{II}(l) = K_{IIc}(l)$, which leads to

$$\sqrt{\frac{l_c}{L}} = \sqrt{\frac{l}{L}}\left[\frac{\tau_N^{\max}}{\mu_k\sigma_N}\left(\frac{4}{\pi}\frac{l}{L}-1\right)+\frac{2}{\pi\mu_k}\frac{F_S}{F_N}\frac{L}{l}-1\right] \tag{13}$$

where $l_c = K_{IIc}^2/(\pi\tau_d^2)$ is a characteristic interface length, and the dynamic interface traction is given by the friction law as $\tau_d = \mu_k\sigma_N = \mu_k F_N/L$.

The characteristic length is in our parameter domain much smaller than the interface length. Therefore, we can write $\sqrt{l_c/L} \approx 0$, and Eq. 13 becomes

$$\frac{F_S}{F_N} = \frac{\pi\mu_k}{2}\frac{l}{L}+\frac{\tau_N^{\max}}{\sigma_N}\frac{l}{L}\left(\frac{\pi}{2}-2\frac{l}{L}\right). \tag{14}$$

With this simplifications, the macroscopic force ratio depends nonlinearly on the normalized precursor length and is controlled by two parameters: the kinetic friction coefficient μ_k and the Poisson's expansion effect τ_N^{max}/σ_N. Note that this prediction neglects all stress redistributions, as in models A and AB. The evolution of $l/L - F_S/F_N$ from Eq. 14 is shown in Fig. 5 with $\tau_N^{\max}/\sigma_N = 0.25$ and $\mu_k = 0.45$ (thick red curve). The scaling compares well

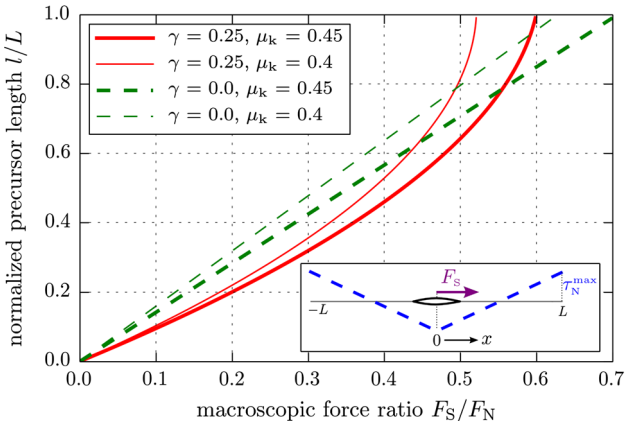

Fig. 5 Precursor load–length relation of minimalistic model for various values of $\gamma = \tau_N^{\max}/\sigma_N$ and μ_k. If the effect of frustrated Poisson's expansion is removed ($\gamma = 0$), then the precursor length increases linearly with the macroscopic force ratio. Generally, a smaller kinetic friction coefficient leads to longer precursors for a given macroscopic shear load. (*inset*) Geometry and loading of minimalistic model

with its equivalent of model A (see Fig. 4c). If shear tractions due to frustrated Poisson's expansion are eliminated ($\tau_N^{\max} = 0$), Eq. 14 predicts a linear load–length relation with a proportionality factor $\pi\mu_k/2$. This prediction (green curve in Fig. 5) can be related to the almost linear evolution of model AB. The kinetic friction coefficient μ_k appears in this scaling, whereas other interface parameters were neglected through the assumption that the characteristic length is much smaller than the interface ($l_c \ll L$). As already observed for the full LEFM theory, its influence on the load–length curve is obvious (compare thin with thick lines in Fig. 5), and small values of μ_k lead to longer precursors for given F_S/F_N.

3.4 LEFM Prediction for Symmetric Setup

Up to this point, we have compared our model to existing experimental data, analyzed the influence of different material and interface parameters, and have studied the nonlinearity of the precursor load–length relation. Now, we can use our LEFM model to predict the response of a different system for which no experimental data has been published yet.

The setup studied so far consists of a thin slider on a thicker base, which presents characteristics of a bi-material interface due to differences in the effective stiffness. This bi-material property influences the rupture propagation [31]. It is potentially interesting to remove this effect from experimental observations of frictional precursors by using a setup with a single-material interface. We thus consider a symmetric system, where the base has the same geometry as the slider (in all three directions) and provide first insights to the propagation of precursors along a single-material interface. In this system, the nonzero τ_N due to frustrated Poisson's expansion (see Fig. 1b) is naturally eliminated. Also all other interface traction components are different in a symmetric setup and are computed with additional static finite-element simulations. An example of an effective normalized contact pressure of the symmetric setup is shown in Fig. 6a (solid pink line) and compared with the normalized contact pressure of the reference setup (dashed blue line), which was already reported in Fig. 1d. As expected, the main difference is the absence of the edge singularity in the symmetric setup at $x/L > 0.9$, which will only have a small influence on the precursor mechanics. In Fig. 6b, the normalized shear traction at the interface of the symmetric setup (solid pink line) and the reference setup (dashed blue line) are compared. The symmetric setup is generally a system of lower stiffness, which leads to a peak at approximately $x/L = 0.05$ that is smaller than in the reference setup but a stress level that is considerably higher up to $x/L = 0.7$.

The precursor load–length prediction of our LEFM model for the symmetric setup is shown in Fig. 6c (pink stars) and

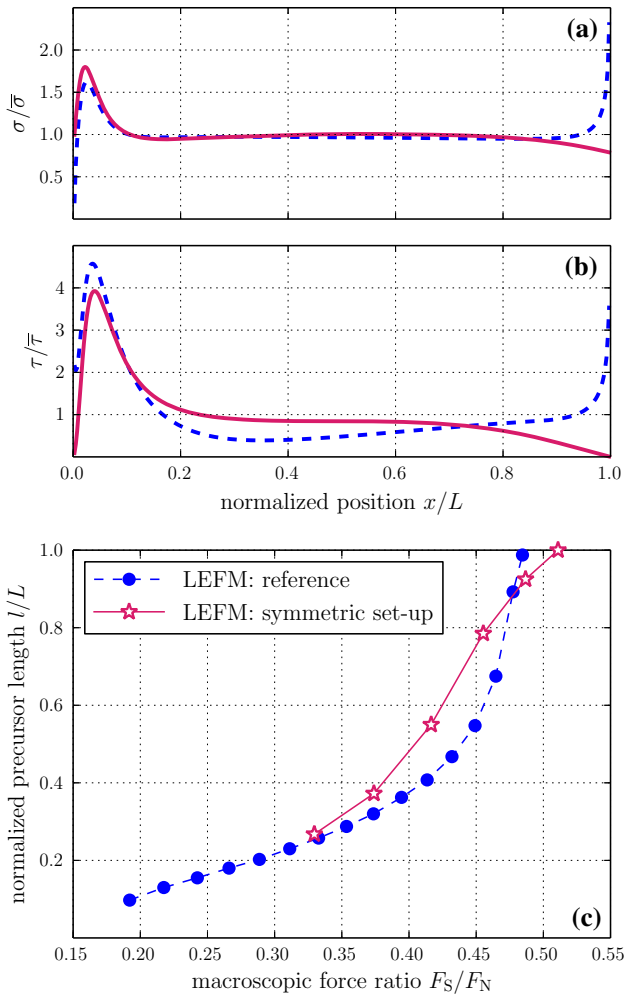

Fig. 6 Comparison with a symmetric setup, where the base has the same geometry as the slider. **a** Normalized contact pressure and **b** normalized shear traction of an unruptured interface for the reference setup (*blue dashed line*), as also shown in Fig. 1d, and for a symmetric setup (*pink solid line*) for $F_N = 5F_S$. **c** Normalized precursor length l/L reported with respect to the macroscopic force ratio F_S/F_N for the reference setup (*blue dots*), as also shown in Fig. 4, and for the symmetric setup (*pink stars*) (Color figure online)

compared with the prediction for the reference system (blue dots), which was already shown in Fig. 4. In the symmetric setup, the first precursor appears at higher macroscopic force ratio, which is the result of the lower stress peak in $\tau_r(x)$ (see Fig. 6b). The length of the first precursor is about the same than the precursor propagating at the same F_S/F_N in the reference system. However, the precursor lengths increase faster in the symmetric system and the load–length relation presents an inflection point between the third and fourth precursors. Moreover, there are considerably less precursors in the prediction for the symmetric setup (precursor length increments are larger), which indicates that it is harder to experimentally observe precursors in such a system.

4 Conclusion

We showed that a theoretical model based on LEFM predicts quantitatively well the precursor behavior observed in laboratory experiments [1]. Using this model, we showed that the kinetic friction coefficient is a key to an accurate prediction of the precursor length as it directly affects the stress intensity factor through the stress drop along the interface crack. Moreover, we showed that the variation of material parameters (within their uncertainty range) does not affect the observed precursor load–length relation. By simplifying this model in various ways, we analyzed different aspects that influence the nonlinearity of the precursor growth and demonstrated that the shear tractions due to frustrated Poisson's expansion and the discrete nature of precursors are the main sources of the observed nonlinearity. The redistribution of the shear tractions along the interface caused by each precursor is essential to the load–length relation. With the results of this theoretical description of slip precursors, we provide evidence for considering frictional slip and precursors as a fracture phenomenon.

Acknowledgments The research described in this article is supported by the European Research Council (ERCstg UFO-240332) and the Swiss National Science Foundation (grant PMPDP2-145448). JPA was funded by US NSF (grant EAR-1015704).

References

1. Rubinstein, S., Cohen, G., Fineberg, J.: Dynamics of precursors to frictional sliding. Phys. Rev. Lett. **98**(22), 226103 (2007). doi:10.1103/PhysRevLett.98.226103
2. Maegawa, S., Suzuki, A., Nakano, K.: Precursors of global slip in a longitudinal line contact under non-uniform normal loading. Tribol. Lett. **38**(3), 313 (2010). doi:10.1007/s11249-010-9611-7
3. Scheibert, J., Dysthe, D.K.: Role of friction-induced torque in stick-slip motion. Europhys. Lett. **92**(5), 54001 (2010). doi:10.1209/0295-5075/92/54001
4. Trømborg, J., Scheibert, J., Amundsen, D., Thøgersen, K., Malthe-Sørenssen, A.: Transition from static to kinetic friction: insights from a 2D model. Phys. Rev. Lett. **107**(7), 074301 (2011). doi:10.1103/PhysRevLett.107.074301
5. Bouchbinder, E., Brener, E.A., Barel, I., Urbakh, M.: Slow cracklike dynamics at the onset of frictional sliding. Phys. Rev. Lett. **107**(23), 235501 (2011). doi:10.1103/PhysRevLett.107.235501
6. Amundsen, D.S., Scheibert, J., Thøgersen, K., Trømborg, J., Malthe-Sørenssen, A.: 1D model of precursors to frictional stick-slip motion allowing for robust comparison with experiments. Tribol. Lett. **45**(2), 357 (2012). doi:10.1007/s11249-011-9894-3
7. Kammer, D.S., Yastrebov, V.A., Spijker, P., Molinari, J.F.: On the propagation of slip fronts at frictional interfaces. Tribol. Lett. **48**(1), 27 (2012). doi:10.1007/s11249-012-9920-0
8. Otsuki, M., Matsukawa, H.: Systematic breakdown of Amontons' law of friction for an elastic object locally obeying Amontons' law. Sci. Rep. **3**, 1586 (2013). doi:10.1038/srep01586
9. Lapusta, N., Rice, J.R.: Nucleation and early seismic propagation of small and large events in a crustal earthquake model. Geophys J. Res. Solid Earth **108**(B4) (2003). doi:10.1029/2001JB000793

10. Wu, Y., Chen, X.: The scale-dependent slip pattern for a uniform fault model obeying the rate-and state-dependent friction law. J. Geophys. Res. Solid Earth **119**(6), 4890 (2014). doi:10.1002/2013JB010779
11. Rubinstein, S.M., Cohen, G., Fineberg, J.: Cracklike processes within frictional motion: is slow frictional sliding really a slow process? MRS Bull. **33**(12), 1181 (2008). doi:10.1557/mrs2008.249
12. Freund, L.B.: The mechanics of dynamic shear crack propagation. J. Geophys. Res. Solid Earth **84**(B5), 2199 (1979). doi:10.1029/JB084iB05p02199
13. Ampuero, J.P., Ripperger, J., Mai, P.M.: In: Abercrombie, R., McGarr, A., Di Toro, G., Kanamori, H. (eds.) Earthquakes: Radiated Energy and the Physics of Faulting, pp. 255–261. American Geophysical Union, Washington, DC (2006). doi:10.1029/170GM25
14. Kato, N.: Fracture energies at the rupture nucleation points of large interplate earthquakes. Earth Planet. Sci. Lett. **353–354**(0), 190 (2012). doi:10.1016/j.epsl.2012.08.015
15. Svetlizky, I., Fineberg, J.: Classical shear cracks drive the onset of dry frictional motion. Nature **509**, 205 (2014). doi:10.1038/nature13202
16. Palmer, A.C., Rice, J.R.: The growth of slip surfaces in the progressive failure of over-consolidated clay. Proc. R. Soc. Lond. A **332**(1591), 527 (1973). doi:10.1098/rspa.1973.0040
17. Andrews, D.: Rupture propagation with finite stress in antiplane strain. J. Geophys. Res. **81**(20), 3575 (1976). doi:10.1029/JB081i020p03575
18. Braun, O., Barel, I., Urbakh, M.: Dynamics of transition from static to kinetic friction. Phys. Rev. Lett. **103**(19), 194301 (2009). doi:10.1103/PhysRevLett.103.194301
19. Kaneko, Y., Ampuero, J.P.: A mechanism for preseismic steady rupture fronts observed in laboratory experiments. Geophys. Res. Lett. **38**(21), L21307 (2011). doi:10.1029/2011GL049953
20. Bar Sinai, Y., Brener, E.A., Bouchbinder, E.: Slow rupture of frictional interfaces. Geophys. Res. Lett. **39**(3), L03308 (2012). doi:10.1029/2011GL050554
21. Bar-Sinai, Y., Spatschek, R., Brener, E.A., Bouchbinder, E.: On the velocity-strengthening behavior of dry friction. J. Geophys. Res. Solid Earth **119**(3), 1738 (2014). doi:10.1002/2013JB010586
22. Radiguet, M., Kammer, D.S., Gillet, P., Molinari, J.F.: Survival of heterogeneous stress distributions created by precursory slip at frictional interfaces. Phys. Rev. Lett. **111**(16), 164302 (2013). doi:10.1103/PhysRevLett.111.164302
23. Radiguet, M., Kammer, D.S., Molinari, J.F.: The role of viscoelasticity on heterogeneous stress fields at frictional interfaces. Mech. Mater. **80**, 276 (2015). doi:10.1016/j.mechmat.2014.03.009
24. Freund, L.: Dynamic Fracture Mechanics. Cambridge University Press, New York (1990)
25. Tada, H., Paris, P.C., Irwin, G.R.: The Stress Analysis of Cracks Handbook, 3rd edn. ASME, New York (2000)
26. Rice, J.R.: In: Kelly, R. (ed.): Proceedings of the Eighth U.S. National Congress of Applied Mechanics. Western Periodicals Co., North Hollywood, California, pp. 191–216 (1979)
27. Uenishi, K., Rice, J.R.: Universal nucleation length for slip-weakening rupture instability under nonuniform fault loading. J. Geophys. Res. **108**(B1), B12042 (2003). doi:10.1029/2001JB001681
28. Garagash, D.I., Germanovich, L.N.: Nucleation and arrest of dynamic slip on a pressurized fault. J. Geophys. Res. **117**(B10), B10310 (2012). doi:10.1029/2012JB009209
29. Ciccotti, M., Mulargia, F.: Differences between static and dynamic elastic moduli of a typical seismogenic rock. Geophys. J. Int. **157**(1), 474 (2004). doi:10.1111/j.1365-246X.2004.02213.x
30. Ben-David, O., Cohen, G., Fineberg, J.: The dynamics of the onset of frictional slip. Science **330**(6001), 211 (2010). doi:10.1126/science.1194777
31. Weertman, J.: Unstable slippage across a fault that separates elastic media of different elastic constants. J. Geophys. Res. **85**(B3), 1455 (1980). doi:10.1029/JB085iB03p01455